

Neutron background measurements with a hybrid neutron detector at the Kuo-Sheng Reactor Neutrino Laboratory

A. Sonay,^{1,2} M. Deniz,^{1,2,*} H. T. Wong,^{2,†} M. Agartioglu,^{1,2} G. Asryan,² J. H. Chen,² S. Kerman,^{1,2} H. B. Li,² J. Li,³ F. K. Lin,² S. T. Lin,^{2,4} B. Sevda,^{1,2} V. Sharma,^{2,5} L. Singh,^{2,5} M. K. Singh,^{2,5} M. K. Singh,^{2,5} V. Singh,⁵ A. K. Soma,^{2,5} S. W. Yang,² Q. Yue,⁶ I. O. Yildirim,⁷ and M. Zeyrek⁷

(The TEXONO Collaboration)

¹ Department of Physics, Dokuz Eylül University, Buca, İzmir TR35390, Turkey

² Institute of Physics, Academia Sinica, Taipei 115, Taiwan

³ Institute of High Energy Physics, Chinese Academy of Science, Beijing 100039, China

⁴ College of Physical Science and Technology, Sichuan University, Chengdu 610064, China

⁵ Department of Physics, Institute of Science, Banaras Hindu University, Varanasi 221005, India

⁶ Department of Engineering Physics, Tsinghua University, Beijing 100084, China

⁷ Department of Physics, Middle East Technical University, Ankara TR06800, Turkey

(Dated: April 27, 2022)

We report *in situ* neutron background measurements at the Kuo-Sheng Reactor Neutrino Laboratory (KSNL) by a hybrid neutron detector (HND) with a data size of 33.8 days under identical shielding configurations as during the neutrino physics data taking. The HND consists of BC-501A liquid and BC-702 phosphor powder scintillation neutron detectors, which is sensitive to both fast and thermal neutrons, respectively. Neutron-induced events for the two channels are identified and differentiated by pulse shape analysis, such that background of both are simultaneously measured. The fast neutron fluxes are derived by an iterative unfolding algorithm. Neutron induced background in the germanium detector under the same fluxes, both due to cosmic-rays and ambient radioactivity, are derived and compared with the measurements. The results are valuable to background understanding of the neutrino data at the KSNL. In particular, neutron-induced background events due to ambient radioactivity as well as from reactor operation are negligible compared to intrinsic cosmogenic activity and ambient γ -activity. The detector concept and analysis procedures are applicable to neutron background characterization in similar rare-event experiments.

PACS numbers: 29.30.Hs, 29.40.-n, 28.41.Qb

I. INTRODUCTION

The TEXONO Collaboration [1] is pursuing experimental investigation of neutrino physics [2–5], as well as weakly interacting massive particle (WIMP) dark matter [6], axions [7] and other physics searches beyond-standard-model (BSM) [8] at the Kuo-Sheng Reactor Neutrino Laboratory (KSNL). Quantitative understanding of neutron-induced background and nature of their sources is crucial to these studies.

We report in this article *in situ* measurement of thermal (n_{thermal}) and fast (n_{fast}) neutron background at KSNL under identical shielding configurations as during the various physics data taking. A custom-built hybrid neutron detector (HND), whose characteristics and performances were reported earlier in our previous publication [9], are used for these measurements.

The paper is structured as follows. The features of the HND and the associated pulse shape discrimination (PSD) techniques are summarized in Section II. Data taking at the KSNL is discussed in Section III. Derivation of the internal contaminations of HND are discussed

in Section IV. Results on the measured neutron-induced background in HND, the calculated neutron fluxes as well as the projected background to high-purity germanium detectors (HPGe) at the same location are presented in Section V.

II. HYBRID NEUTRON DETECTOR

The HND is constructed with two different target materials— a Bicorn BC-501A liquid scintillator with a 0.113 liter cell volume and a BC-702 scintillator of thickness 0.6 cm enriched with 95% ^6Li as fine ZnS(Ag) phosphor powder – to be read out by a 5.1 cm diameter photomultiplier (PMT) at the same time. A schematic drawing is shown in Figure 1. As depicted in Figure 2, the HND was installed at the same location as the various HPGe within the well of an NaI(Tl) anti-Compton detector and kept under the same shielding configurations and data taking conditions. The measured ambient neutron flux is therefore the same as what the HPGe were exposed to in the physics data taking.

Different particles produce different pulse shapes with the HND [9]. The normalized reference pulses of α , n_{fast} , n_{thermal} and γ are shown in Figure 3. In Ref. [9], two independent PSD techniques were developed, which are based on the parameter of t_{PSD} , derived from the ratio

*Corresponding Author: muhammed.deniz@deu.edu.tr

†Corresponding Author: ht Wong@phys.sinica.edu.tw

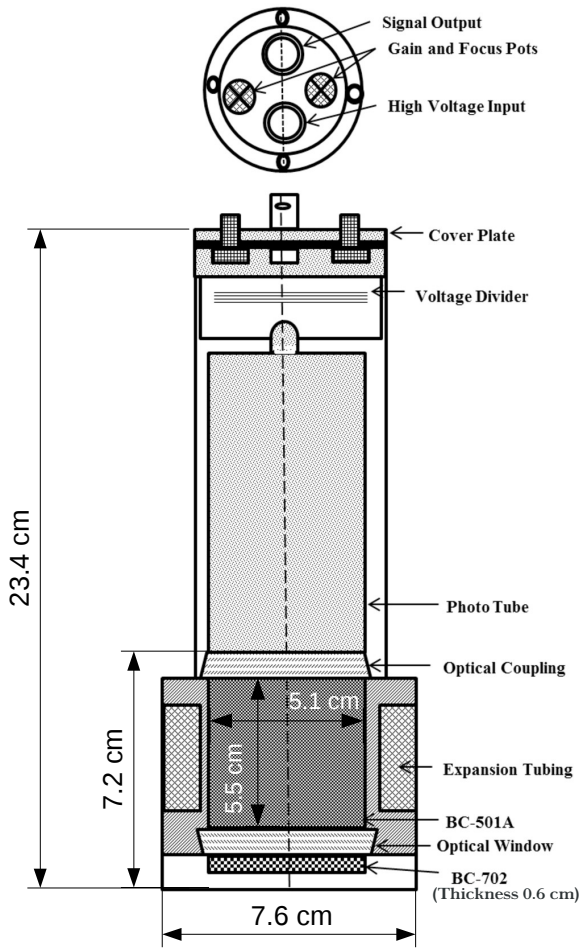


FIG. 1: Schematic diagram of the HND.

of partial (Q_p) to total (Q_t) integration of the pulses, and based on the B/A ratio of individual pulses given as

$$t_{PSD} = \frac{Q_p}{Q_t} = \frac{I[(t_{20} + 50ns) : (t_{20} + 150ns)]}{I[(t_{20}) : (t_{20} + 150ns)]}$$

$$L = A \times (e^{-\theta(t-t_0)} - e^{-\lambda_s(t-t_0)}) + B \times (e^{-\theta(t-t_0)} - e^{-\lambda_l(t-t_0)}), \quad (1)$$

where I denotes integration of the pulse area and t_{20} represents the time where the pulses reach 20% of the amplitude. Here L represents the pulse shape, A and B are the normalization constants, t_0 is reference time and θ , λ_s , and λ_l represent decay constants. Different particles are identified by different B/A ratios for a specific scintillator.

For this study, a reference pulse is constructed by adopting ^{60}Co as the γ source. The parameters of decay constants θ , λ_s , λ_l and reference time t_0 are obtained from the fitting of the γ reference pulse. The pulse shape

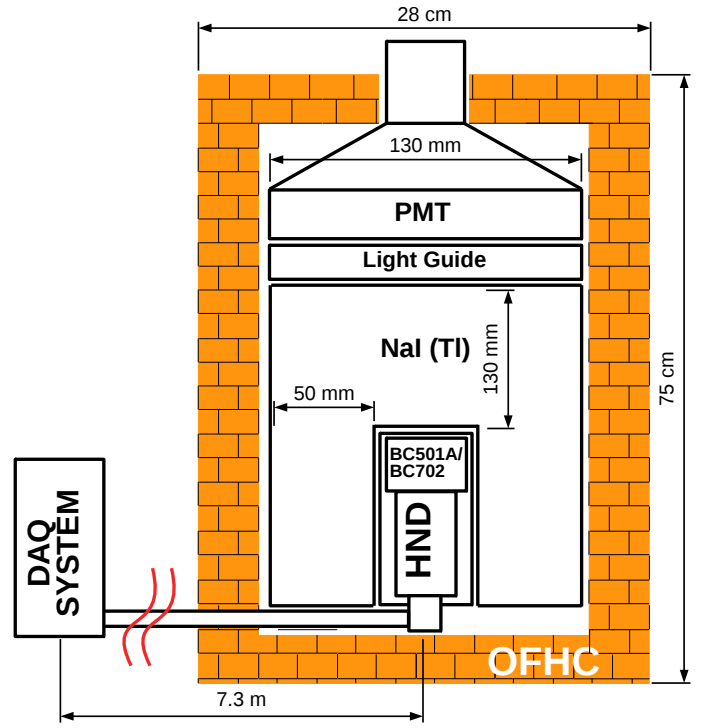


FIG. 2: Schematic view of experimental setup inside the 50 ton shielding structure (not shown). Signals are brought to the DAQ system via cables of 7.3 m in length.

is then parameterized as,

$$L = A \times \left[(e^{-(t-0.52)/226.6} - e^{-(t-0.52)/17.23}) + 0.115 \times (e^{-(t-0.52)/226.6} - 1) \right], \quad (2)$$

where t is in ns-unit, and A is the only free normalization parameter that remains to be determined [9]. Individual pulses are fitted with the function given in Eq. 2 in order to identify γ against neutron events.

The $^{241}\text{AmBe}(\alpha, n)$ and $^{60}\text{Co}-\gamma$ sources are used as reference for the t_{PSD} and B/A PSD techniques, respectively. Adopting the PSD parameters given in Eq. 1 and Eq. 2, three spectral bands corresponding to γ , fast and slow neutron components of the events can be observed, as depicted in Figure 4.

III. DATA TAKING AT KUO-SHENG NEUTRINO LABORATORY

Several HPGe-based measurements [2, 4–8] have been carried out at KSNL. The external dimensions of the HND were selected to resemble those of HPGe. Data were taken at KSNL with the HND placed at the same location as the HPGe [1] under identical active and passive shielding configurations, as depicted in Figure 2. The plastic scintillator panels function as cosmic-ray vetos (CR) while the well-shaped

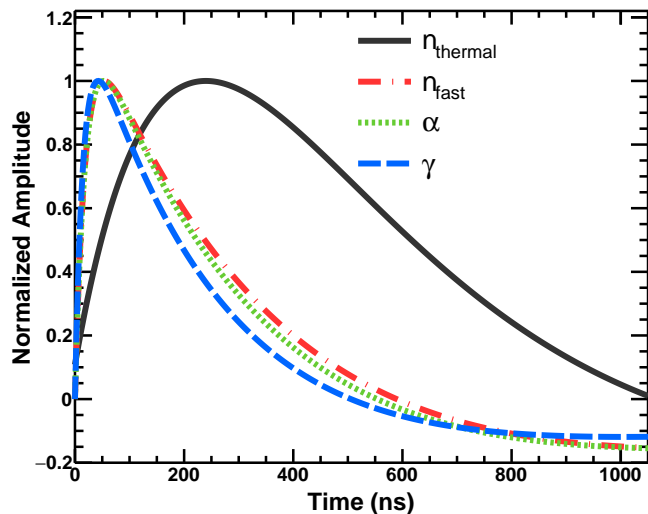


FIG. 3: Reference pulse shapes for γ - n_{fast} - and n_{thermal} -induced events from the HND, from which PSD techniques are devised to differentiate them. Pulse shapes of fast neutrons and alpha-particles are very close and in practice not distinguishable.

NaI(Tl) serves as an anti-Compton (AC) detector, and in its cavity the HND (HPGe in early experiments) was placed. The HND+NaI(Tl) detectors were further shielded by oxygen-free high-conductivity (OFHC) copper and placed inside a sealed volume with nitrogen gas flow as a purge of the radioactive radon gas. The setup was installed inside a 50 ton shielding structure [1] consisting of, from inside out, OFHC copper, boron-loaded polyethylene, lead and CR panels, for suppression of ambient γ and neutron background, and for tagging cosmic-ray induced events.

The schematic design for the data acquisition (DAQ) system is given in Figure 5. The HND signals above a discriminator threshold provided the triggers. Signals from other detector components were recorded, to be used for the suppression of AC and CR events in subsequent offline analysis. The HND signals were processed by two fast timing amplifiers [10] at different gains and recorded by 8-bit flash-analog-to-digital converters [11] at 1 GHz sampling time. Data taking period lasted more than a month and a total of 33.8 live-time days of data were collected for subsequent analysis.

The goal of offline analysis is to categorize the events and determine their respective energy spectra. After standard filtering of events due to electronic noise and other spurious non-physical triggers, the physical events are identified as $(\gamma, n_{\text{fast}}, n_{\text{thermal}})$ from the reference pulse shape information as in Figure 4. The origins of these events are derived from the AC and CR detectors according to four categories: $\text{CR}^{\pm} \otimes \text{AC}^{\pm}$ where $+(-)$ denotes coincidence (anti-coincidence) of the CR or AC with HND. In particular, the $\text{CR}^+ \otimes \text{AC}^-$ tag selects CR neutron-induced events, the $\text{CR}^- \otimes \text{AC}^+$ tag is rich in

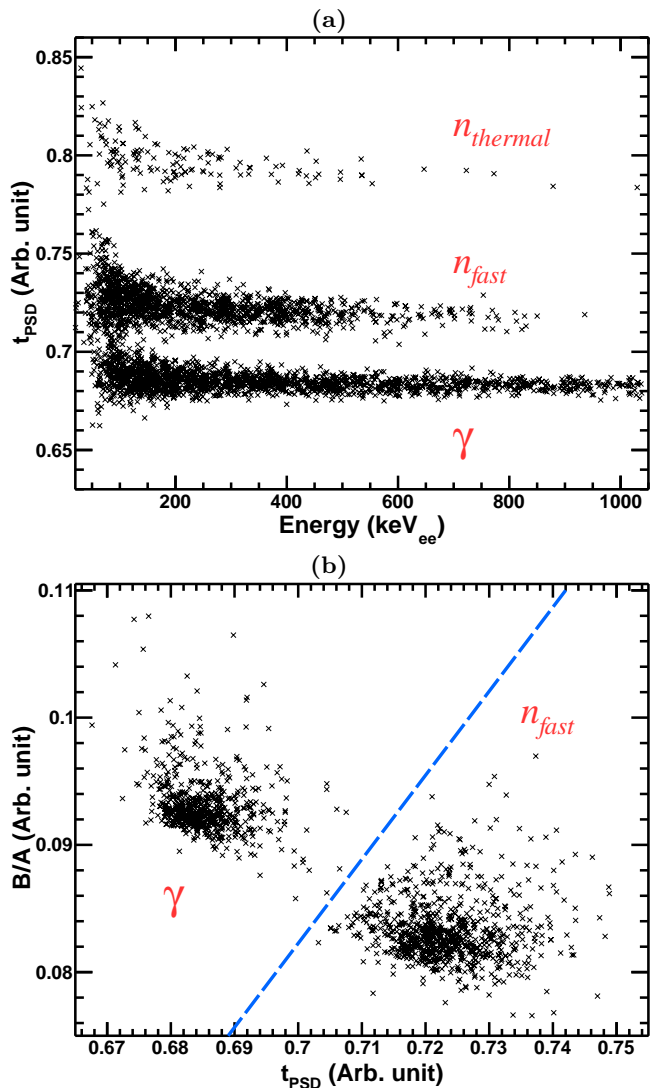


FIG. 4: PSD techniques devised to differentiate γ - n_{fast} - and n_{thermal} -induced events, based on (a) t_{PSD} , and (b) B/A ratio developed in Ref. [9].

ambient γ -induced AC events, while $\text{CR}^- \otimes \text{AC}^-$ is the condition for selecting neutrino- or WIMP-induced candidate events uncorrelated with both CR and AC systems.

IV. INTERNAL CONTAMINATION OF NEUTRON DETECTOR

The measurement of intrinsic radiopurity of the HND is essential for determining the ambient neutron background, especially those in $\text{CR}^- \otimes \text{AC}^-$. Nuclear α -decays from the ^{238}U and ^{232}Th series can mimic neutron-induced nuclear recoil signatures, and hence their contributions must be determined.

The PSD characteristics of α -events as well as the unique time correlations of two decay sequences (DS)

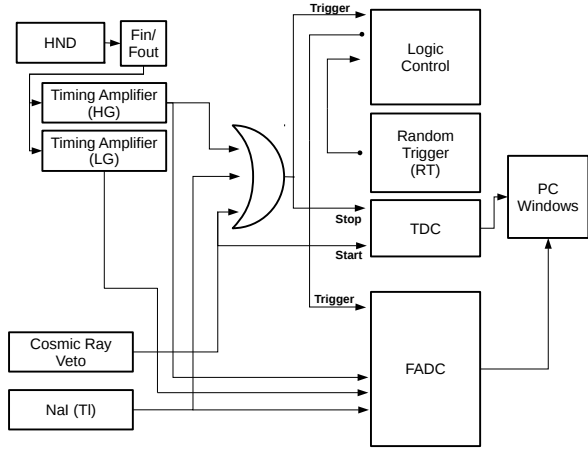


FIG. 5: Schematic diagram of the data acquisition system.

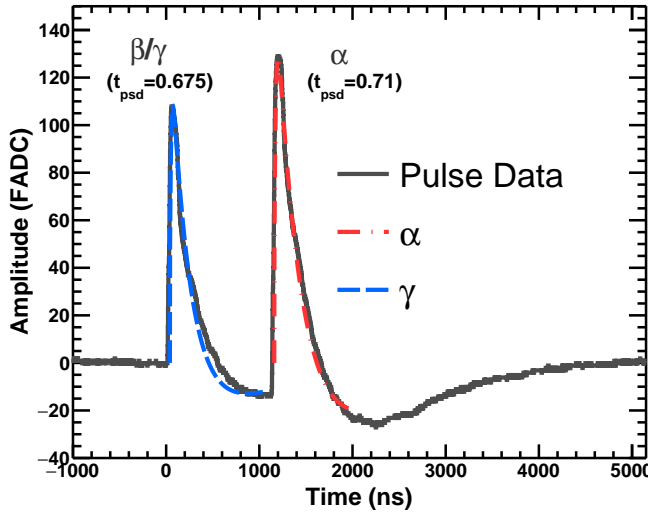
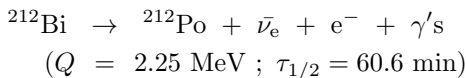


FIG. 6: A typical double-pulse event in $CR^- \otimes AC^-$ channel.

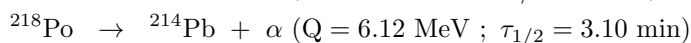
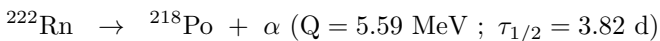
provide powerful means to measure contaminations of the ^{232}Th and ^{238}U series, from which the α -background can be evaluated, assuming secular equilibrium.

The related DS are [12]:

DS₁: Within the ^{232}Th series, there is 64% branching ratio for ^{212}Bi to decay via a β - α cascade –



DS₂: Within the ^{238}U series, there is α - α cascade from ^{222}Rn –



Typical example of a double pulse event is displayed in Figure 6, interpreted as a β – α cascade based on PSD. A collection of the delayed pulses in similar cascades provide the α reference pulse shape as shown in Figure 3. The n_{fast}/γ events are distinguishable while n_{fast}/α events are not distinguishable in an event-by-event basis since the differences in their pulse shapes are smaller than electronic fluctuations.

The delay-time (Δt) distributions for the correlated-events from $DS_{1,2}$ are shown in Figure 7(a) and Figure 7(b), respectively. Results of best-fit parameters to exponential decay functions are displayed in Table I.

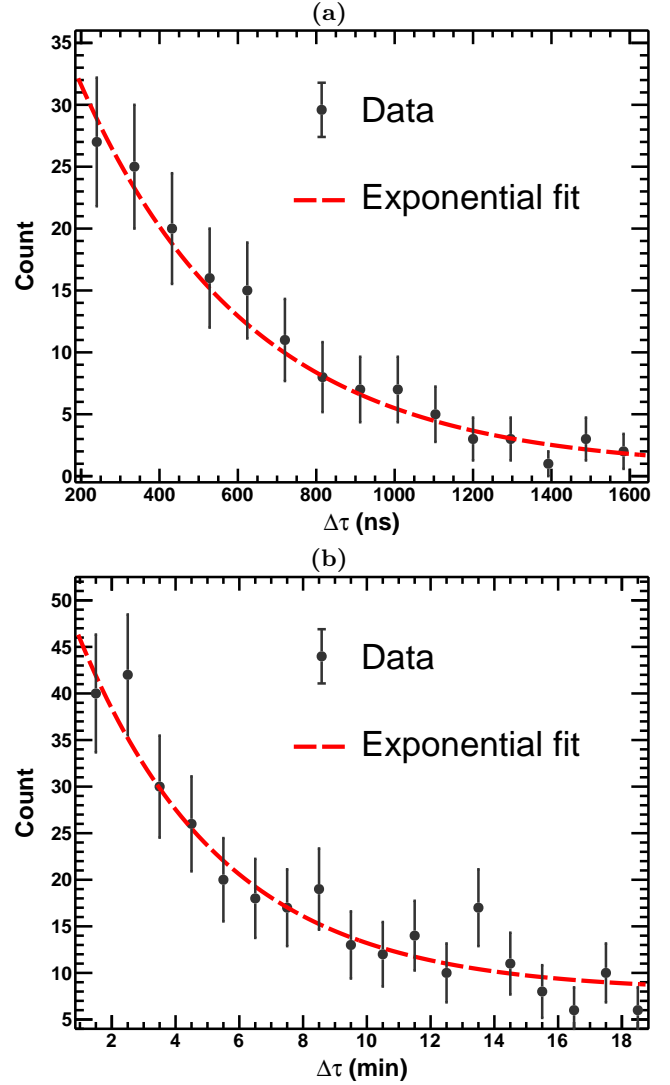


FIG. 7: Distribution for (a) β - α events from $^{212}\text{Bi} \rightarrow ^{212}\text{Po} \rightarrow ^{208}\text{Pb}$ in DS_1 , (b) α - α events from $^{222}\text{Rn} \rightarrow ^{218}\text{Po} \rightarrow ^{214}\text{Pb}$ in DS_2 .

The measured event rate of the decay sequences of $DS_{1,2}$ can be used for the estimation of contamination levels of their long-lived parent isotopes of ^{232}Th and ^{238}U in the detector. Simulated α energy spectra of ^{232}Th

TABLE I: Summary of measured values and inferred radioactivity levels of the two cascade sequences.

Series	DS ₁	DS ₂
	²³² Th	²³⁸ U
Signatures	β - α	α - α
Decays	²¹² Bi \rightarrow ²¹² Po \rightarrow ²⁰⁸ Pb	²²² Rn \rightarrow ²¹⁸ Po \rightarrow ²¹⁴ Pb
χ^2 /n.d.f	4.7/16	9.0/17
Half-Life		
Nominal	299 ns	3.10 min
Measured	302 \pm 27 ns	3.14 \pm 0.39 min
Counts in 33.8 days	366.20 \pm 26.94	292.50 \pm 15.43
Radioactivity (mBq/kg)	0.140 \pm 0.010	0.110 \pm 0.006
Contaminations $\times 10^{-11}$ (g/g)	2.21 \pm 0.16	0.89 \pm 0.048

and ²³⁸U series, convoluted with detector resolution and quenching effects are depicted in Figure 8.

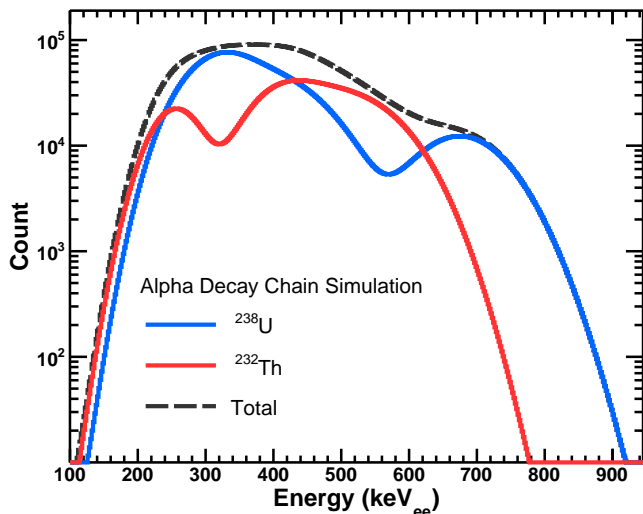


FIG. 8: Simulated α energy spectrum of ²³²Th and ²³⁸U decay chains including detector resolution and quenching effects [9]. Normalization is fixed by the measured cascade sequences of Table I.

The measured half-lives are consistent with nominal values. The measured event rates can be translated to the radioactivity and contamination levels of their long-lived parent isotopes of ²³²Th and ²³⁸U in the detector, assuming secular equilibrium. Simulated α energy spectra of ²³²Th and ²³⁸U parent isotopes convoluted with detector resolution and quenching effects are depicted in Figure 8.

V. NEUTRON BACKGROUND

A. Thermal neutron background

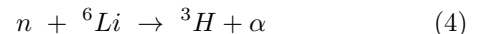
Thermal neutrons are those with kinetic energy below 1 eV and in thermal equilibrium with the ambient surroundings. Their energy distribution is described by the Maxwell-Boltzmann distribution with a most probable energy of $E_{th} \sim 0.02$ eV, which corresponds to a velocity of $v_{th} \sim 2200$ ms⁻¹.

The scintillator BC-702 used for thermal neutron measurements does not provide energy information of the incident neutron. Calculation of the thermal neutron flux is performed assuming Maxwell-Boltzmann distributions.

For a neutron flux $\phi_n(E)$ with interaction cross-section $\sigma(E)$ in the detector, the count rate in the detector is given by:

$$R_{th} = N \int \sigma(E) \phi_n(E) dE, \quad (3)$$

where N is the total number of target nuclei in the detector. The thermal neutron capture by ⁶Li in HND



is inversely proportional to the neutron velocity $v(E)$, such that

$$\sigma(E) = \sigma_{th} \frac{v_{th}}{v(E)}, \quad (5)$$

where $\sigma_{th} = 940$ b. An isotropic and homogeneous flux distribution can be described by

$$\phi(E) = v(E) \rho_n(E), \quad (6)$$

where $\rho_n(E)$ is the neutron number density at energy E in the detector volume. The count rate can therefore be expressed as

$$R_{th} = N \sigma_{th} v_{th} \langle \rho_n \rangle, \quad (7)$$

where $\langle \rho_n \rangle$ is the energy-averaged thermal neutron number density. The averaged neutron velocity is given by

$$\langle v \rangle = \frac{\int v(E) \rho_n(E) dE}{\int \rho_n(E) dE} = \frac{\Phi}{\langle \rho_n \rangle}, \quad (8)$$

where Φ is the total flux. Accordingly, the rate becomes

$$R_{th} = N \sigma_{th} \frac{v_{th}}{\langle v \rangle} \Phi. \quad (9)$$

Maxwell-Boltzmann distribution for thermal neutrons gives rise to the relation

$$\frac{\langle v \rangle}{v_{th}} = \frac{2}{\sqrt{\pi}}. \quad (10)$$

Accordingly, the total neutron flux is related to the measured count rate by

$$\Phi_n = \frac{2R_{th}}{N\sigma_{th}\sqrt{\pi}}. \quad (11)$$

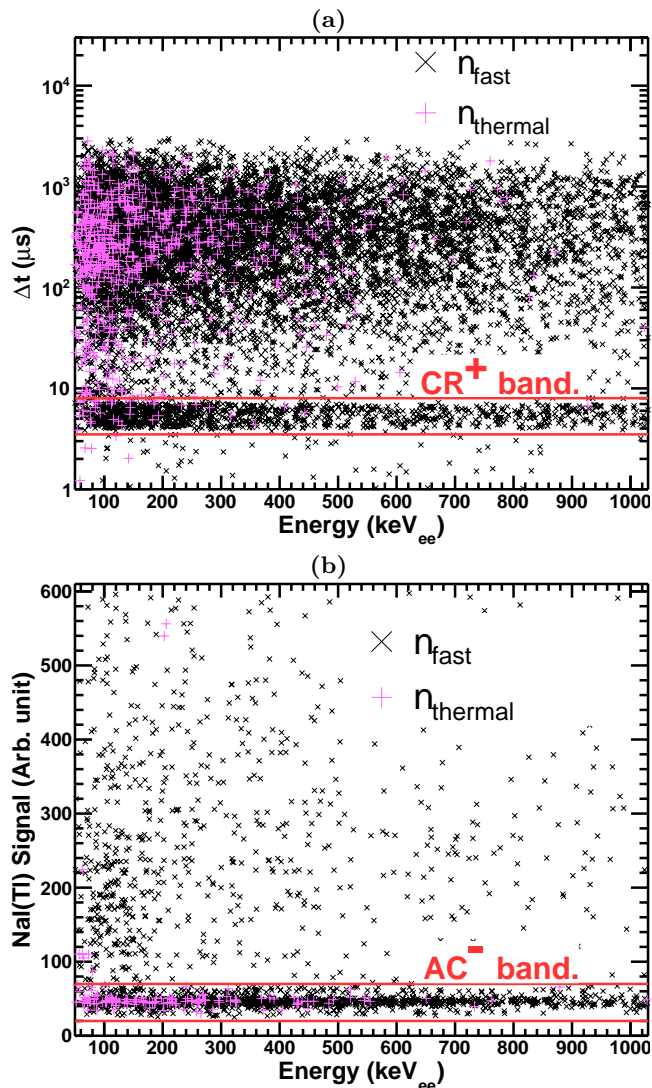


FIG. 9: Event selection criteria for (a) cosmic-ray CR^+ , and (b) anti-Compton AC^- events, showing most thermal neutrons are with $\text{CR}^- \otimes \text{AC}^-$ tag.

The measured thermal neutron rate at KSNL with HND BC-702 is

$$R_{th} = (4.15 \pm 0.12) \times 10^{-4} \text{ counts s}^{-1} . \quad (12)$$

With a total number of $N = 1.41 \times 10^{22}$ ${}^6\text{Li}$ atoms in BC-702 [13, 14], the corresponding total thermal neutron flux is

$$\Phi_n = (3.54 \pm 0.10) \times 10^{-5} \text{ cm}^{-2} \text{ s}^{-1} . \quad (13)$$

The majority of the thermal neutron events are with $\text{CR}^- \otimes \text{AC}^-$ tag uncorrelated with the other detector systems, as depicted in Figure 9. The time difference between these events with the previous CR^+ tag is displayed in Figure 10, in which accidental coincidence from

random trigger events are superimposed. An excess is observed with a correlation time scale of about $200 \mu\text{s}$, indicating that part (20%) of thermal neutron capture events can be matched to the thermalization of specific cosmic-ray events.

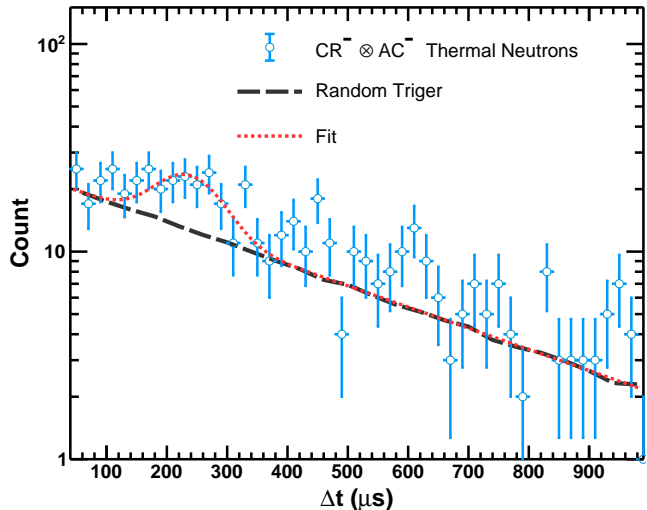


FIG. 10: The time difference between $\text{CR}^- \otimes \text{AC}^-$ thermal neutron and the previous cosmic-ray events. Comparison with random trigger events up to $\sim 400 \mu\text{s}$ indicate that about 20% of thermal neutrons can be matched to their parent cosmic-ray events.

B. Measured nuclear recoil spectra; Evaluated fast neutron flux; Projected HPGe background

Once the HND spectra are measured, unfolding algorithms as discussed in Ref. [9], followed by a Friedman smoothing algorithm [15], are applied to produce the corresponding fast neutron spectra. The expected nuclear recoil background in HPGe detectors at the same location and shielding configurations are then evaluated with full GEANT simulation [16] and compared with 173.5-kg-days of data taken under identical passive and active shielding configurations with an n-type point-contact germanium detector [17]. Standard quenching function of Ge [17] are used to convert nuclear recoil energy in keV_{nr} into the observable energy in electron-equivalence unit keV_{ee} .

Results with $\text{CR}^+ \otimes \text{AC}^-$ samples are displayed in Figure 11, in which (a) is the recoil spectrum from the HND liquid scintillator, (b) is the evaluated neutron spectrum and (c) is the projected Ge recoil spectrum from the same neutron background. The fast neutron spectrum has a threshold at $700 \text{ keV}_{\text{nr}}$ due to HND response. The threshold effects give rise to a change of slope of the Ge-recoil spectrum at $4 \text{ keV}_{\text{ee}}$, below which the predicted spectrum is less than the measured one. This excesses can be corrected for with an extrapolation to the neutron

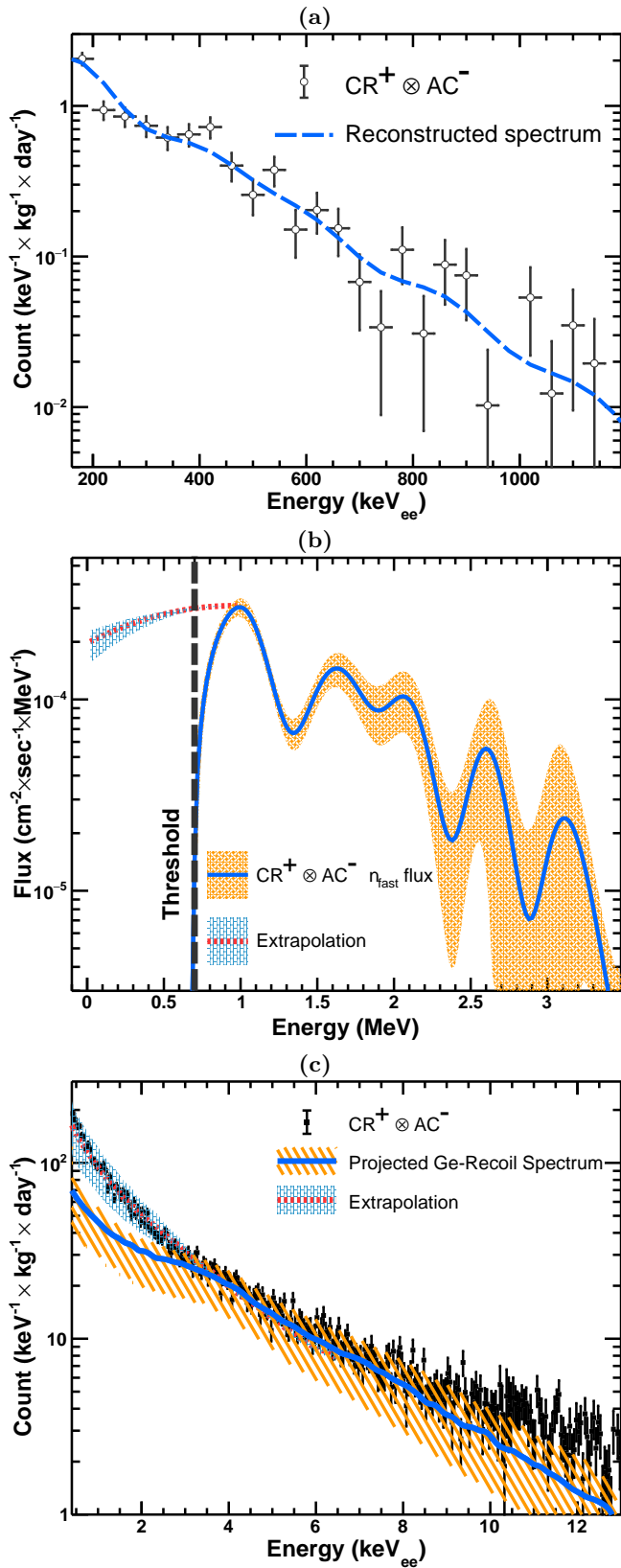


FIG. 11: The sample of $\text{CR}^+ \otimes \text{AC}^-$ – (a) HND nuclear recoil energy spectrum, (b) unfolded neutron flux with $\pm 1\sigma$ error as shadow area, (c) the comparison of HPGe data and predicted Ge-recoil spectrum from simulations with the measured neutron fluxes. Extrapolated spectra of (b) and (c) at low energy, as fixed by neutron flux models of Figure 16 derived from equilibrium yield of ${}^{70}\text{Ge}(n,\gamma){}^{71}\text{Ge}$, are corrections to the effects due to finite HND threshold of 150 keV_{ee} .

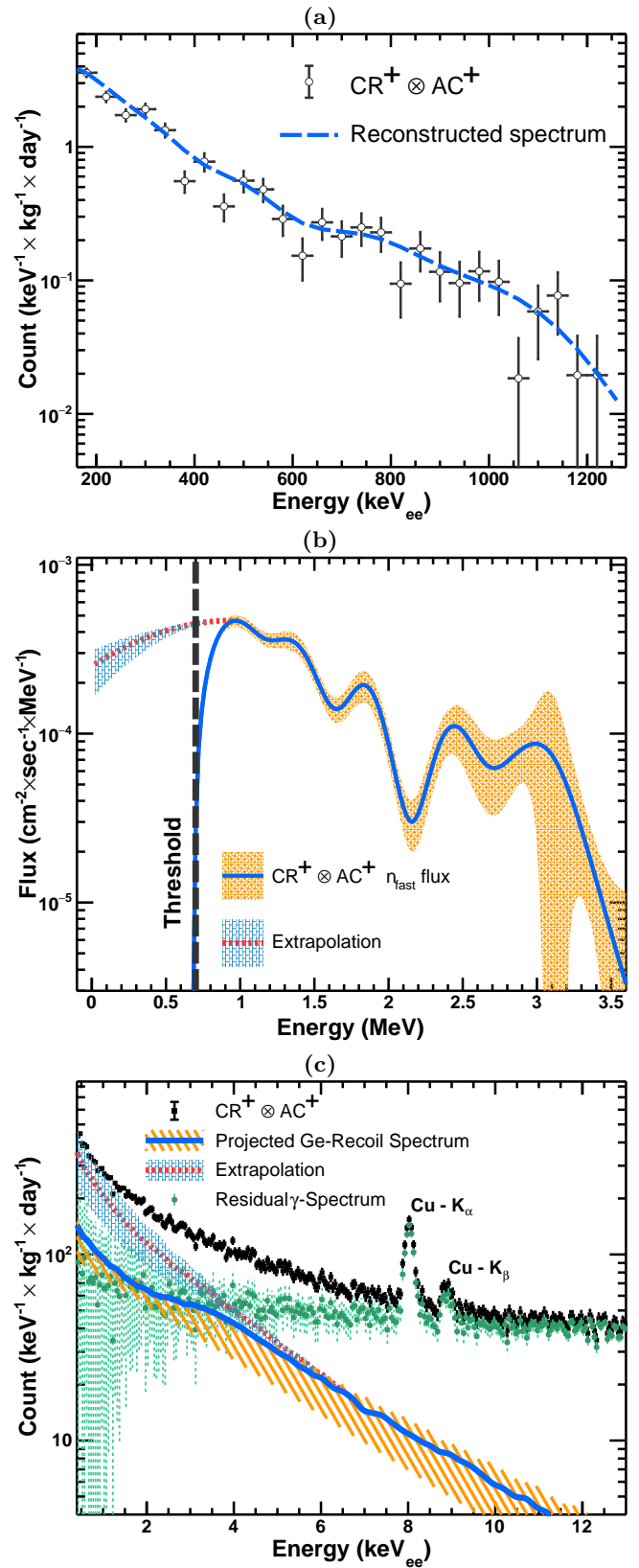


FIG. 12: The sample of $\text{CR}^+ \otimes \text{AC}^+$ – (a) HND nuclear recoil energy spectrum, (b) unfolded neutron flux with $\pm 1\sigma$ error as shadow area, (c) the comparison of HPGe data and predicted Ge-recoil spectrum from simulations with the measured neutron fluxes. Extrapolated spectra of (b) and (c) at low energy, as fixed by neutron flux models of Figure 16 derived from equilibrium yield of ${}^{70}\text{Ge}(n,\gamma){}^{71}\text{Ge}$, are corrections to the effects due to finite HND threshold of 150 keV_{ee} .

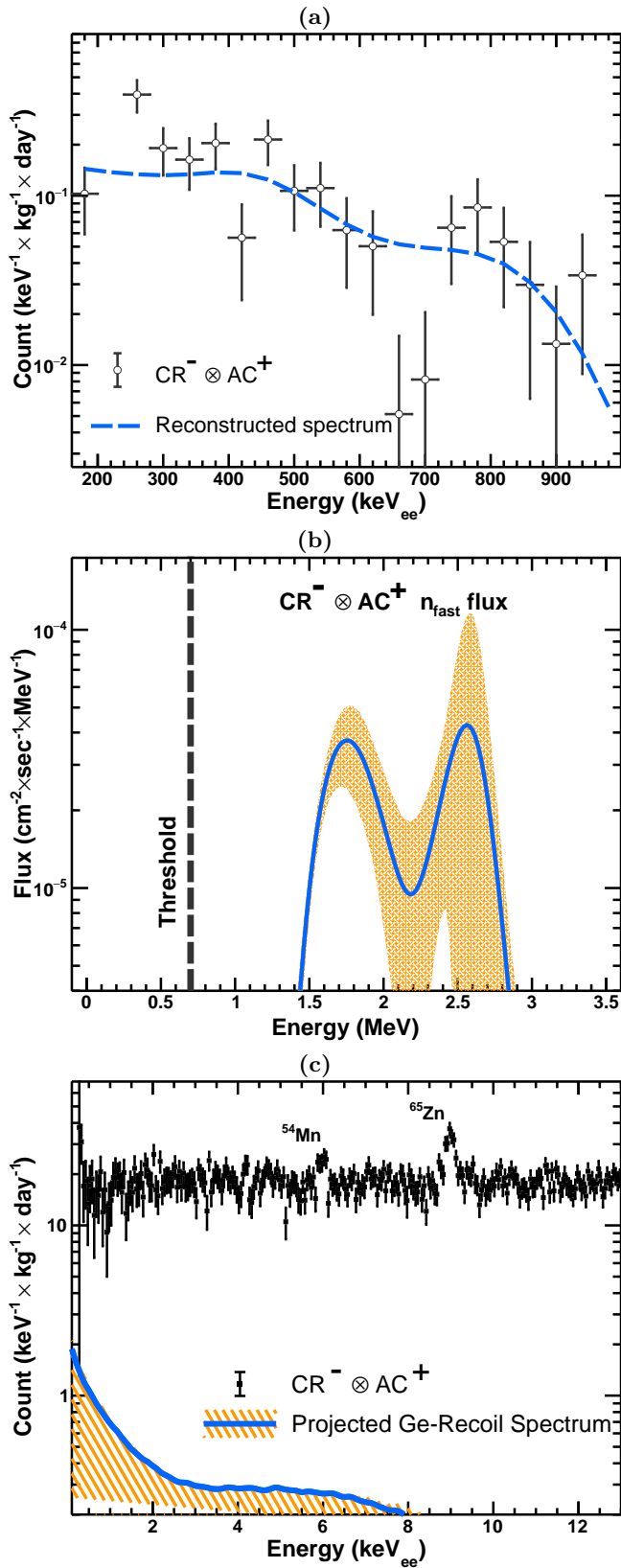


FIG. 13: The sample of $\text{CR}^- \otimes \text{AC}^+$ – (a) HND nuclear recoil energy spectrum, (b) unfolded neutron flux with $\pm 1\sigma$ error as shadow area, (c) the comparison of HPGe data and predicted Ge-recoil spectrum from simulations with the measured neutron fluxes.

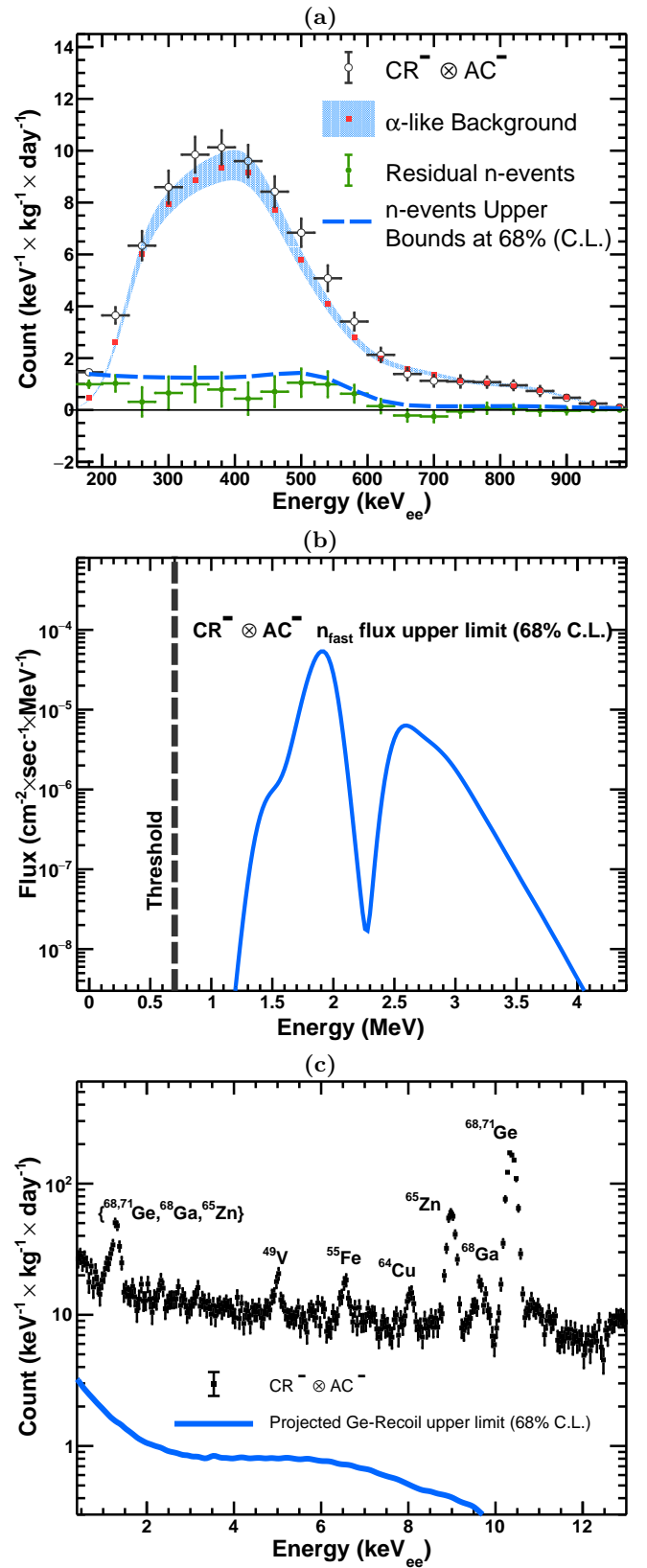


FIG. 14: The sample of $\text{CR}^- \otimes \text{AC}^-$ – (a) energy spectra for HND nuclear recoil-like events, together with the measured α -background from ^{232}Th and ^{238}U decay series and the 68% C.L. upper bound of neutron-induced nuclear recoils, from which the upper bounds of (b) unfolded neutron spectrum and (c) predicted Ge-recoil background in HPGe can be derived and compared with measured data.

flux, the procedures and details of which are described in Section V-C.

The same analysis procedures are applied to the $\text{CR}^+ \otimes \text{AC}^+$ samples, and the results presented in Figure 12 follow the same convention. There exists a finite residual spectrum after the Ge-recoils are accounted for, as depicted in Figure 12c. The residual events are due to Compton scattering of cosmic-ray induced high energy ambient γ -rays, characterized by a flat spectrum and consistent with simulations. The two peaks corresponds to copper K_α and K_β X-ray emission lines produced by the interactions of cosmic-ray muons with the copper support materials in the vicinity of the active Ge crystal.

Similarly, the results of the cosmic-ray anti-coincidence samples with $\text{CR}^- \otimes \text{AC}^+$ and $\text{CR}^- \otimes \text{AC}^-$ tags are displayed in Figure 13 and Figure 14, respectively. It can be seen from Figure 13(c) and Figure 14(c), in both cases that neutron-induced Ge-recoil events, which are unrelated to cosmic-rays only constitute a minor component relative to that due to ambient γ -radioactivity. The $\text{CR}^- \otimes \text{AC}^-$ events are uncorrelated with CR and AC detectors and represent the physics candidate samples for the studies of neutrino and dark matter. The measured ‘‘recoil-like’’ spectrum can completely be explained by internal α -contaminations as discussed in Section IV, such that only upper bounds for HND and HPGe as well as fast neutron spectra can be derived. The upper limits of these spectra at 68% C.L. are displayed in Figure 14. The peaks in both Figure 13(c) and Figure 14(c) are due to X-rays emissions following electron capture (EC) by the unstable isotopes, which are produced by cosmogenic activation of long-lived isotopes inside the HPGe target.

C. Complete Neutron Spectrum

Combining both the measured thermal and fast neutron fluxes and spectra, and adopting the neutron slowing-down theory [18], which is described by a $1/E$ behavior of the epithermal region in between, the complete neutron spectrum at KSNL can be modeled using information of the *in situ* measurements of neutron capture rates.

Figure 15a and Figure 15b show the variations over the whole data taking period (347 days) of the X-ray peaks at 10.37 keV_{ee} and 9.66 keV_{ee} , respectively, following EC of ${}^{71}\text{Ge} + {}^{68}\text{Ge}$ and ${}^{68}\text{Ga}$. These isotopes are primarily produced by neutron capture channels ${}^{70}\text{Ge}(n,\gamma){}^{71}\text{Ge}$ followed by EC in ${}^{71}\text{Ge}(e^-, \nu_e){}^{71}\text{Ga}$ and ${}^{70}\text{Ge}(n,3n){}^{68}\text{Ge}$ followed by ${}^{68}\text{Ge}(e^-, \nu_e){}^{68}\text{Ga}$ and ${}^{68}\text{Ga}(e^-, \nu_e){}^{68}\text{Zn}$.

The decreasing intensities with time are consequences of less *in situ* cosmogenic activation compared to the pre-installation activities. The measured lifetimes are consistent with nominal values and the equilibrium levels displayed in Table II, on the other hand, provide information on the *in situ* neutron capture rates of ${}^{70}\text{Ge}$, and hence the neutron fluxes. The level of 9.66 keV_{ee} line is consistent with zero, which reveals that *in situ* pro-

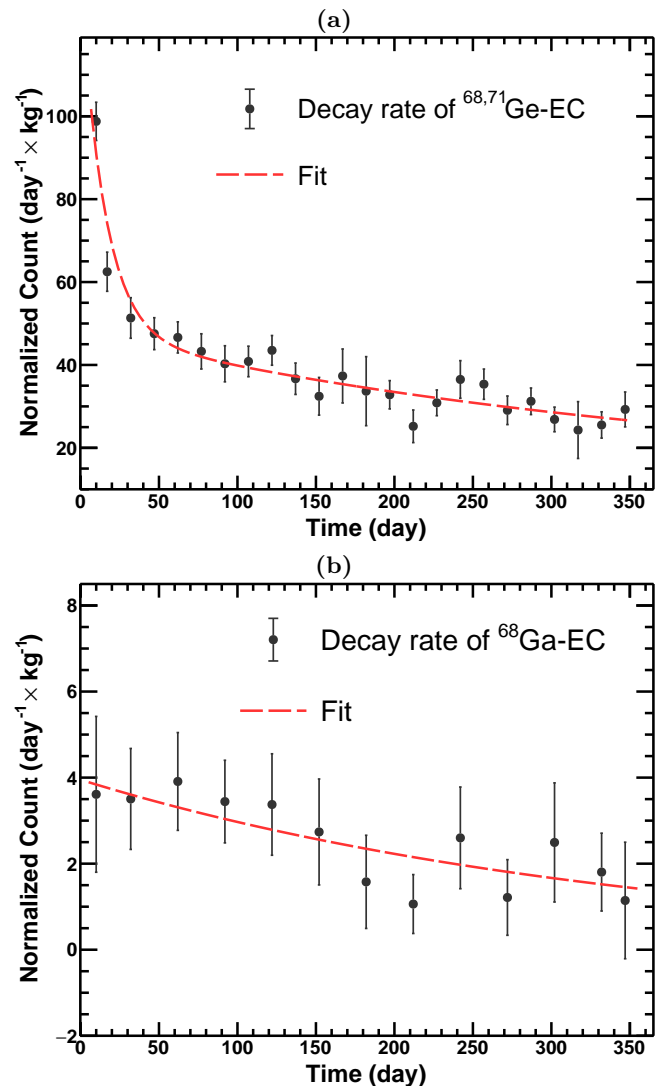


FIG. 15: Time variation of characteristic K X-ray lines of (a) ${}^{71}\text{Ge}$ and ${}^{68}\text{Ge}$, and (b) ${}^{68}\text{Ga}$. Exponential best-fits are superimposed.

duction of ${}^{70}\text{Ge}(n,3n){}^{68}\text{Ge}$ is negligible. According to TENDL nuclear data library [19], the threshold for the production of ${}^{70}\text{Ge}(n,3n){}^{68}\text{Ge}$ is 20 MeV. The production of ${}^{68}\text{Ge}$ is therefore negligible at KSNL, where the maximum measured neutron energy is 5 MeV. This expectation is supported by the measurement of Figure 15b, where the equilibrium yield of the 9.66 keV_{ee} line and hence *in situ* production of ${}^{70}\text{Ge}(n,3n){}^{68}\text{Ge}$ are consistent with zero. Accordingly, the equilibrium yield of the 10.37 keV_{ee} line is due exclusively to *in situ* production of ${}^{70}\text{Ge}(n,\gamma){}^{71}\text{Ge}$. This measured rate is used to fix the normalization of the epithermal neutron component.

The complete neutron background spectrum at KSNL is displayed in Figure 16. The capture rates of ${}^{70}\text{Ge}(n,3n){}^{68}\text{Ge}$ and ${}^{70}\text{Ge}(n,\gamma){}^{71}\text{Ge}$ due to the thermal, epithermal and fast neutron components evaluated by

TABLE II: Summary of the *in situ* measured $^{71}\text{Ge}/^{68}\text{Ge}$ (10.37 keV $_{ee}$) and ^{68}Ga (9.66 keV $_{ee}$) characteristic K X-ray line rates at KSNL – for both transient and in equilibrium components. The equilibrium rates provide information of the *in situ* yields for $^{70}\text{Ge}(n,\gamma)^{71}\text{Ge}$ and $^{70}\text{Ge}(n,3n)^{68}\text{Ge}$, both of which are in excellent agreement with simulation predictions using neutron flux model of Figure 16 as input.

Channel (K X-ray Lines)	Half-Life ($\tau_{1/2}$)(day)		Rate (kg $^{-1}$ day $^{-1}$)
	Nominal	Measured	
Measurements			
^{71}Ge from Transient 10.37 keV $_{ee}$	11.43	10.63 ± 1.08	2.70 ± 0.90
^{68}Ge from Transient 10.37 keV $_{ee}$	270.95	275.76 ± 9.01	23.9 ± 6.4
^{68}Ge from Transient 9.66 keV $_{ee}$	270.95	246.74 ± 46.16	2.2 ± 0.6
Equilibrium 9.66 keV $_{ee}$ = $[^{70}\text{Ge}(n,3n)^{68}\text{Ge}]$			< 0.39 (68% C.L.)
Equilibrium 10.37 keV $_{ee}$ = $[^{70}\text{Ge}(n,\gamma)^{71}\text{Ge} + ^{70}\text{Ge}(n,3n)^{68}\text{Ge}]$			12.40 ± 3.70
Simulated Predictions (kg $^{-1} \times \text{day}^{-1}$)			$^{70}\text{Ge}(n,\gamma)^{71}\text{Ge}$
n_{thermal}			8.05 ± 0.23
$n_{\text{epithermal}}$			2.18 ± 0.67
n_{fast}			3.67 ± 1.50
Total			13.90 ± 1.65

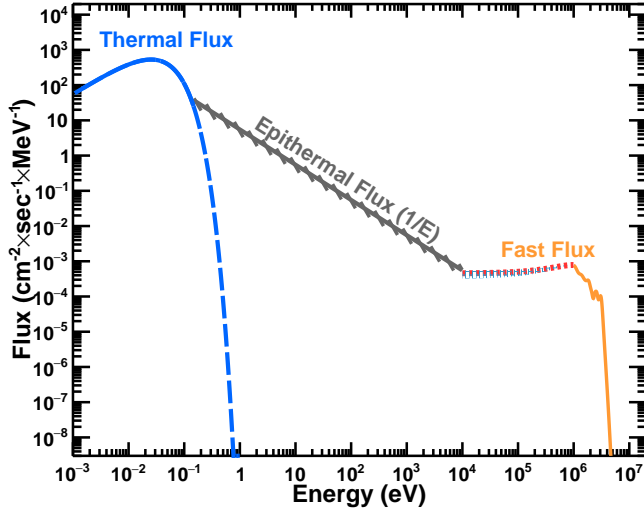


FIG. 16: Neutron spectrum model at the target region of KSNL. The total thermal and fast neutron components are based on measurements and analysis reported in this article. The epithermal component is from interpolation.

full GEANT simulations [16] are listed in Table II, the sum of which is in excellent agreement with the measured rates. The consistency is illustrated in the measured $\text{CR}^- \otimes \text{AC}^-$ HPGe spectra of Figure 17 in which the different contributions to the Ge K X-ray lines are shown. Their total fluxes under different tags are given in Table III.

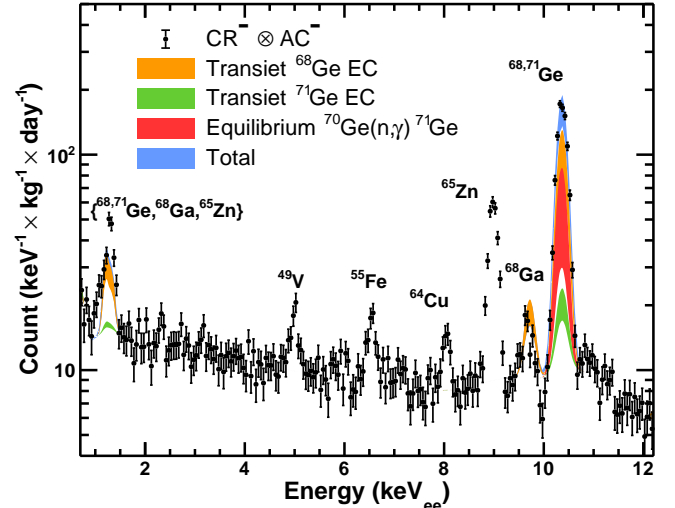


FIG. 17: Measured $\text{CR}^- \otimes \text{AC}^-$ spectrum with HPGe at KSNL. The various contributions to the ^{71}Ge , ^{68}Ge characteristic K X-ray, L X-ray lines and the ^{68}Ga K X-ray line, based on predictions using the measured equilibrium neutron capture rates, are superimposed.

Once the complete neutron background is modeled, the cut-off effects of the fast neutron spectra around 700 keV in Figure 11(b) and Figure 12(b) due to the HND threshold at 150 keV $_{ee}$ can be corrected for by of the neutron spectra to lower energy. The corrected Ge-recoil spectra with the additional neutrons taken into account are

TABLE III: Summary of flux measurements of different categories of neutrons.

Neutrons	Measured Fluxes
	Φ_n ($\text{cm}^{-2}\text{s}^{-1}$)
Thermal – 0.02 eV – 1.00 eV	
$\text{CR}^+ \otimes \text{AC}^-$	$(2.68 \pm 0.28) \times 10^{-6}$
$\text{CR}^+ \otimes \text{AC}^+$	$(3.00 \pm 0.29) \times 10^{-6}$
$\text{CR}^- \otimes \text{AC}^+$	$(9.33 \pm 1.65) \times 10^{-7}$
$\text{CR}^- \otimes \text{AC}^-$	$(2.87 \pm 0.09) \times 10^{-5}$
Epithermal	$\begin{cases} > 4.39 \times 10^{-5} \\ < 8.25 \times 10^{-5} \end{cases}$
Fast – 0.70 MeV – 4.00 MeV	
$\text{CR}^+ \otimes \text{AC}^-$	$(2.35 \pm 1.60) \times 10^{-4}$
$\text{CR}^+ \otimes \text{AC}^+$	$(4.53 \pm 2.29) \times 10^{-4}$
$\text{CR}^- \otimes \text{AC}^+$	$(1.49 \pm 5.75) \times 10^{-6}$
$\text{CR}^- \otimes \text{AC}^-$	$< 3.22 \times 10^{-6}$

displayed in Figure 11(c) and Figure 12(c). The corrected $\text{CR}^+ \otimes \text{AC}^-$ Ge-recoil spectrum provides a perfect (>99%) match to the measured data, confirming the expected physical picture where $\text{CR}^+ \otimes \text{AC}^-$ samples are dominated by nuclear recoil events due to interactions of cosmic-ray induced fast neutrons. Similarly, the corrected $\text{CR}^+ \otimes \text{AC}^+$ Ge-recoil spectrum has the expected exponential decrease with energy. Once accounted for, the residual cosmic-induced γ -background is flat down to sub-keV, also expected from Compton scattering of high energy γ -rays. The consistencies of these independent measurements serve as non-trivial cross-checks on the validity of neutron flux measurements as well as the experimental approaches and analysis procedures reported in this work.

VI. SUMMARY AND PROSPECTS

We report in this article *in situ* measurements of neutron-induced background at KSNL with a HND under identical active and passive shielding configurations during the neutrino physics measurements. The differ-

ent components of neutron fluxes thus derived are summarized in Table III, and the neutron spectrum is depicted in Figure 16. The derived neutron spectrum provides excellent agreement with the cosmic-ray neutron-induced Ge-recoil spectra as shown in Figure 11(c) and Figure 12(c), thereby providing strong support to the validity of the results as well as the experimental approaches and analysis procedures.

It was demonstrated that elastic nuclear recoil events due to cosmic-ray induced high energy neutrons contribute almost exclusively to the $\text{CR}^+ \otimes \text{AC}^-$ channel below 12 keV_{ee}, and are major components of the $\text{CR}^+ \otimes \text{AC}^+$ channel, dominating over γ -induced background below 4 keV_{ee}. On the other hand, contributions of cosmic-uncorrelated neutrons to the background are minor in $\text{CR}^- \otimes \text{AC}^+$ and unobservable in $\text{CR}^- \otimes \text{AC}^-$. In particular, the dominant background to the studies of neutrinos, WIMP dark matter and axions with $\text{CR}^- \otimes \text{AC}^-$ selection at KSNL are ambient γ -radioactivity and intrinsic cosmogenic activation. Contributions of neutrons from ambient radioactivity and reactor operation are negligible, a feature consistent with expectations from full GEANT simulations. The HND detector concept and analysis procedures can be applicable to characterize neutron background in other rare-event experiments, in both surface and underground laboratories. In particular, the equilibrium levels of the X-ray peaks in HPGe detectors can be used to measure *in situ* background neutron fluxes. This technique can be extended to other Ge-based underground WIMP-search experiments[20–22].

VII. ACKNOWLEDGMENTS

This work is supported by Contract No. 114F374 under Scientific and Technological Research Council of Turkey (TUBITAK), the Academia Sinica Principal Investigator Award, Contract No. 104-2112-M-001-038-MY3 from the Ministry of Science and Technology, Taiwan and Contract No. 2017-ECP2 from the National Center of Theoretical Sciences, Taiwan. M.K. Singh thanks the University Grants Commission (UGC), Govt. of India, for the funding through UGC D.S. Kothari Postdoctoral Fellowship (DSKPDF) scheme (No. F. 4-2/2006 (BSR)/PH/15-16/0098).

[1] H.T. Wong, The Universe Vol. 3, No.4, 22-37 (2015).
[2] H.B. Li *et al.*, Phys. Rev. Lett. **90**, 131802 (2003).
[3] M. Deniz *et al.*, Phys. Rev. D **81**, 072001 (2010).
[4] J.W. Chen *et al.*, Phys. Rev. D **90**, 011301(R) (2014).
[5] H.T. Wong *et al.*, J.Phys.Conf.Ser.39:266-268,2006; S. Kerman *et al.*, Phys. Rev. D **93**, 113006 (2016).
[6] S.T. Lin *et al.*, Phys. Rev. D **79**, 061101(R) (2009); H.B. Li *et al.*, Phys. Rev. Lett. **110**, 261301 (2013).

[7] H.M. Chang *et al.*, Phys. Rev. D **75**, 052004 (2007).
[8] M. Deniz *et al.*, Phys. Rev. D **82**, 033004 (2010); S. Bilmiş *et al.*, Phys. Rev. D **85**, 073011 (2012); S. Bilmiş, I. Turan, T.M. Aliev, M. Deniz, L. Singh, and H.T. Wong, Phys. Rev. D **92**, 033009 (2015); M. Deniz *et al.*, Phys. Rev. D **95**, 033008 (2017); B. Seveda *et al.*, Phys. Rev. D **96**, 035017 (2017).
[9] M.K. Singh *et al.*, Nucl. Instr. and Meth. A **868**, 109

- (2017).
- [10] Canberra 2111 timing amplifier, data sheet available at http://phy.fiu.edu/pub/TWiki/MAST_Diagnostic/Equipment_Amplifier.pdf.
- [11] National instruments, PXI-5154 FADC, data sheet available at <http://www.ni.com/pdf/manuals/376291b.pdf>.
- [12] S.Y.F. Chu, L.P. Ekstrom and R.B. Firestone, The Lund/LBNL Nuclear Data Search, <http://nucleardata.nuclear.lu.se/toi/>.
- [13] J.B. Birks, The theory and practice of scintillation counting, Pergamon Press (1964).
- [14] BC-702 data sheet available at, https://www.crystals.saint-gobain.com/sites/imdf.crystals.com/files/documents/sgc-bc702-data-sheet_70148.pdf; BC501-A data sheet available at, https://www.crystals.saint-gobain.com/sites/imdf.crystals.com/files/documents/sgc-bc501-501a-519-data-sheet_69711.pdf.
- [15] J. H. Friedman, California LCS Technical Report No. 5 SLAC PUB-3477, (1974).
- [16] GEANT4 Collaboration - S. Agostinelli, *et. al.* Nucl. Instr. and Meth. A **506**, 250-303 (2003) SLAC-PUB-9350, FERMILAB-PUB-03-339.
- [17] A.K. Soma *et al.*, Nucl. Instr. and Meth. A **836**, 67-82 (2016).
- [18] Y. Oka, “Nuclear Reactor Design”, Springer, **Pg. 52**, (2010); J.R. Lamarsh, “Introduction to Nuclear Reactor Theory” Addison-Wesley, (1966).
- [19] TENDL Nuclear data library at https://tendl.web.psi.ch/tendl_2015/neutron_html/Ge/NeutronGe70residual.html.
- [20] C. E. Aalseth *et. al.*, Phys. Rev. D, **88**, 012002 (2013).
- [21] L.T. Yang *et. al.*, Chin. Phys. C **42**, 23002 (2018); H. Jiang *et. al.*, arXiv:1802.09016 (2018).
- [22] R. Agnese *et. al.*, Phys.Rev. D **97**, no.2, 022002 (2018); R. Agnese *et. al.*, Phys. Rev. Lett. **120**, 061802 (2018).